Applied Radiation and Isotopes

A journal of nuclear and radiation techniques and their applications in the physical, chemical, biological, medical, earth, planetary, environmental and engineering sciences

(This is a sample cover image for this issue. The actual cover is not yet available at this time.)

Contents lists available at SciVerse ScienceDirect

Applied Radiation and Isotopes

journal homepage: www.elsevier.com/locate/apradiso

Synchrotron-based DEI for bio-imaging and DEI-CT to image phantoms with contrast agents

Donepudi V. Rao [a,*], Medasani Swapna [a], Roberto Cesareo [a], Antonio Brunetti [a], Tako Akatsuka [b], Tetsuya Yuasa [b], Zhong Zhong [c], Tohoru Takeda [d], Giovanni E. Gigante [e]

[a] Istituto di Matematica e Fisica, Università degli Studi di Sassari, Via Vienna 2, 07100 Sassari, Italy
[b] Department of Bio-System Engineering, Faculty of Engineering, Yamagata University, Yonezawa, Japan
[c] Brookhaven National Laboratory, National Synchrotron Light Source, Upton, New York, USA
[d] Allied Health Science, Kitasato University 1-15-1 Kitasato, Sagamihara, Kanagawa 228-8555, Japan
[e] Dipartimento di Fisica, Università di Roma, La Sapienza 00185 Roma, Italy

HIGHLIGHTS

▶ Distinguishable anatomical structures features of rat kidney and rat brain are acquired with Sy-DEI in planar mode.
▶ Images of a small brain phantom and cylindrical phantom are acquired in tomography mode (Sy-DEI-CT) with contrast agents.
▶ Sy-DEI and Sy-DEI-CT techniques provide new source of information related to biological microanatomy.

ARTICLE INFO

ABSTRACT

The introduction of water, physiological, or iodine as contrast agents is shown to enhance minute image features in synchrotron-based X-ray diffraction radiographic and tomographic imaging. Anatomical features of rat kidney, such as papillary ducts, ureter, renal artery and renal vein are clearly distinguishable. Olfactory bulb, olfactory tact, and descending bundles of the rat brain are visible with improved contrast.

© 2012 Elsevier Ltd. All rights reserved.

1. Introduction

Synchrotron-based X-ray imaging systems are available at a few light source facilities around the world. Few supporting imaging systems, for example, synchrotron-based diffraction-enhanced imaging system (Sy-DEI) in planar (Chapman et al., 1997) and in tomography (Sy-DEI-CT) (Dilmanian et al., 2000) modes have been developed, utilizing refraction properties. These imaging techniques were widely investigated with applications to low density biological materials to enhance the image contrast. The systems can provide excellent image contrast, when imaging anatomical samples, such as rat's kidney or brain and phantoms containing contrast agents. In recent years, these systems generated high resolution images with considerable improvement in contrast compared to conventional radiographic imaging. In addition, these systems have the ability to measure the phase and amplitude changes of an X-ray wavefront traversing the sample. The generated contrast has been associated with the gradient of the X-ray phase-shift. This phase-shift enhances the contrast of a weakly absorbing sample.

Sy-DEI is a radiographic imaging technique which uses a single-energy fan beam of X-rays, instead of the broad energy beam used in conventional imaging. It utilizes the fine angular acceptance of a diffracting analyzer crystal in such a way that it is possible to create several physically unique images. The fine angular acceptance of Bragg diffraction separates out the components of the X-ray beam that have undergone different interactions within the sample. The analyzer crystal's acceptance

* Corresponding author. Tel.: +39 79229480; fax: +39 79229482.
E-mail address: dvrao@uniss.it.(D.V. Rao)

is described by its rocking curve, which is a plot of reflectivity against the angle of incidence of the X-ray beam on the crystal. The analyzer's rocking curve is key to the separation of diffraction-enhanced images. Depending on the algorithms used it is possible to create apparent absorption, refraction and ultra small-angle scattering (USAS) images. Sy-DEI technique derives contrast from absorption, refraction and extinction. This technique proved to offer great advantages over standard X-ray absorption imaging techniques when imaging soft-tissue (Rao et al., 2003, 2005).

The behavior of X-rays as they traverse through a sample can be described using a complex index of refraction, just as in conventional optics. In the X-ray region, the index of refraction, n, deviates only slightly from unity; it can be written as

$$n = 1 - \delta - i\beta \tag{1}$$

$$\delta = (\lambda^2 r_e / 2\pi) \sum_i N_i (Z_i + f_i') \tag{2}$$

$$\beta = (\lambda^2 r_e / 2\pi) \sum_i N_i f_i'' \tag{3}$$

where 'β' describes the absorption of X-rays and the phase-shift term 'δ' incorporates refractive effects. In Eqs. (2) and (3), 'r_e' is the classical electron radius, 'λ' is the wavelength of the X-ray, 'N_i' is the atomic density of element 'i', 'Z_i' is the atomic number of element 'i', and f_i' and f_i'' are the real and imaginary parts respectively of the anomalous scattering factor of element 'i'.

By using the constituents of the refractive index, the X-ray intensity change $\ln(I/I_0)$, caused by amplitude decrease in a uniform-density sample, is given by

$$\ln(I/I_0) = (-4\pi\beta t/\lambda) \tag{4}$$

and the phase-shift $d\theta$ is given by

$$d\theta = (2\pi\delta t/\lambda) \tag{5}$$

Conventional absorption-contrast X-ray imaging uses $\ln(I/I_0)$ as image contrast, while phase-contrast X-ray imaging uses $d\theta$. Therefore, the sensitivity ratio between absorption and phase-contrast imaging is given by the ratio of (δ/β). Fig. 1 shows the dependence of phase to attenuation contrast ratio for a few biological samples.

Real and imaginary parts of the refractive indices are responsible for the phase-shifts and absorption for enhanced contrast. For biological samples, the real part is up to 1000 times greater than the imaginary part. In this context, phase-sensitive imaging techniques (Fitzgerald, 2000; Wilkins et al., 1996) are more efficient than conventional methods. Its ability to render the images with absorption, refraction and scatter rejection qualities, has allowed the detection of specific soft tissue based on small differences in tissue densities. This novel technique motivated researchers to perform extensive research on various samples in medical, bio-medical, biological and material sciences (Zhong et al., 1997; Chapman et al., 1998; Muehleman et al., 2003; Oltulu et al., 2003; Li et al., 2003; Lewis et al., 2003; Kiss et al., 2004; Rao et al., 2010).

The key to this imaging method is an analyzer crystal placed between the tissue under study and the X-ray detector. The analyzer crystal can differentiate between X-rays that are traveling much less than one ten thousandth of a degree apart. This method of imaging reduces scatter and helps to visualize low-contrast areas that otherwise would be lost. Some examples include, images of rat bone and lumber vertebra (Rao et al.,
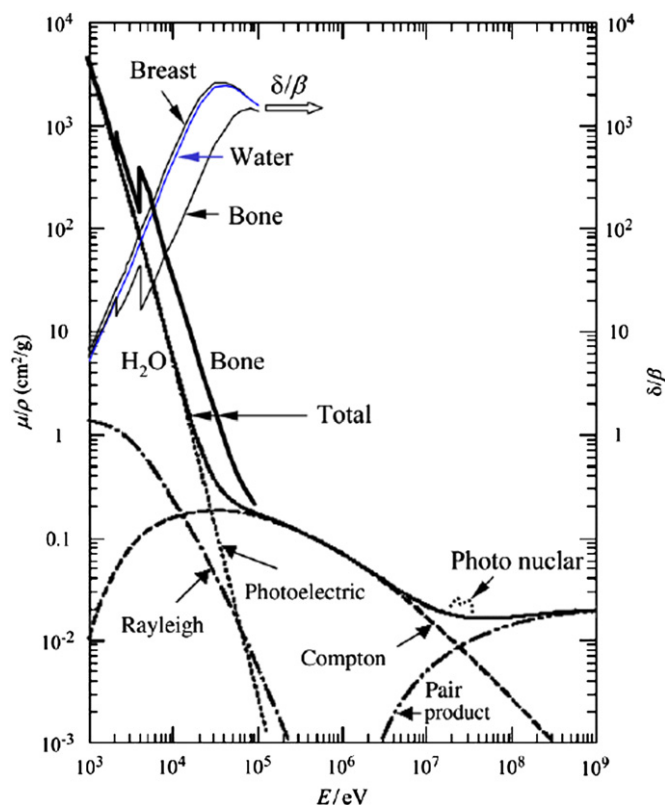

Fig. 1. Dependence of the phase to attenuation contrast parameter ratio (δ/β) for breast tissue, water and cortical bone as well as dependence of the mass attenuation coefficients of water (H_2O) and cortical bone on X-ray photon energy. Here, relevant numerical data are taken from NIST database for X-ray mass attenuation coefficients (Hubbell and Seltzer, 1996). It is seen that the phase-contrast is large at around 20–80 keV for soft tissues.

2005a), rat spine (Kelly et al., 2006), imaging applications (Kim et al., 2006), cartilage damage (Muehleman et al., 2006), ophthalmic diseases (Antunes et al., 2006), controlled defects within bone, including bone–metal gaps (Connor et al., 2006), mass density images (Wernick et al., 2006), multiple-image radiography (Khelashvili et al., 2006; Brankov et al., 2006; Muehleman et al., 2006; Chou et al., 2007), compositional images (Hasnah et al., 2007), images of seeds (Young et al., 2007), and biological soft-tissue images (Rao et al., 2007).

Sy-DEI-CT is another novel X-ray phase-contrast imaging technique, to extract phase information from refraction angle images, from a series of original images measured in different positions of the rocking curve of the analyzer crystal (Zhong et al., 2000). It is difficult to distinguish overlapping structures in 2D image of Sy-DEI. To overcome this problem, we have chosen Sy-DEI-CT to visualize the micro-architecture and minute details with reasonable contrast and spatial resolution, with interior phase information. We imaged a small brain phantom and cylindrical phantom with contrast agents with Sy-DEI-CT, in order to produce pure absorption and refraction images. By utilizing Sy-DEI-CT, considerable enhancement in contrast is achieved, where the effects of refraction and scatter rejection are analyzed by the crystal optics. Light elements, such as hydrogen, carbon, nitrogen and oxygen constitute the soft tissue, resulting in poor contrast images with conventional radiography techniques. Synchrotron-based DEI-CT, imaging is sensitive to light elements, which exhibits excellent imaging property for phase objects. It seems to be an ideal method for imaging rat kidney, rat brain and phantoms with contrast agents (Thomlinson et al., 1998).

2. Experimental methods

2.1. Experimental details

Fig. 2 shows a schematic of the synchrotron radiography facility and the Sy-DEI system available, at, NSLS, BNL, USA, used in this work. More details are given by Zhong et al. (2000). In Sy-DEI-CT imaging, the phantom as placed on a Huber (Blake Industries, Scotch Plains, NJ) rotational stage. Fig. 3(a) shows a photograph of the test brain phantom used. For the other phantom; we used a cylindrical acrylic phantom with variable vertical holes of diameter of 4 mm (Fig. 3b). Fig. 3(c) shows the top view of the cylindrical phantom. Fig. 4. shows the fixation of the sample in Perspex containers filled with water as contrast agent for Sy-DEI planar imaging for the rat kidney and rat brain.

The collimated fan beam of X-rays was produced by a Silicon [3,3,3] monochromator consisting of two perfect silicon crystals. Once this beam passes through the object, a third crystal (analyzer crystal) of the same reflection index diffracts the X-rays onto a radiographic film (Kodak Professional Industrie 150, Industrex SR45) or an image plate detector (Fuji HRV image plate, read out by a Fuji BAS2500 image plate reader at 50 µm pixel size) or a X-ray CCD detector (Photonic Science VHR camera, 9 µm pixel size). The CCD camera was used for the current study. The distance between the X-ray source and the specimen was approximately 15 m while the distance between the specimen and the X-ray detector was about 0.6 m. The pixel size on the image plate reader was set to 50 µm, but it should be noted that the point spread function (PSF) of the image plate has a FWHM value around 141 µm (Kiss et al., 2004). The point spread function is a potentially significant factor in the detectability of small details in the present samples.

For planar radiographic imaging, the image is formed by scanning the sample and detector at the same speed through the fan beam, in approximately opposite directions to take account of the inversion of the beam by Bragg reflection by the analyzer crystal. Because of the non-dispersive nature of the crystals, the narrow Darwin-width of the diffraction used, and the small distance between the sample and the detector, the resolution of the image obtained is limited by the resolution of the detector which is about 15 µm for this study.

The Bragg condition for the analyzer crystal is met only when the incident beam makes the correct angle with the lattice planes in the crystal for a given X-ray energy. When this condition is met, the beam diffracts from the planes over a narrow range of incident
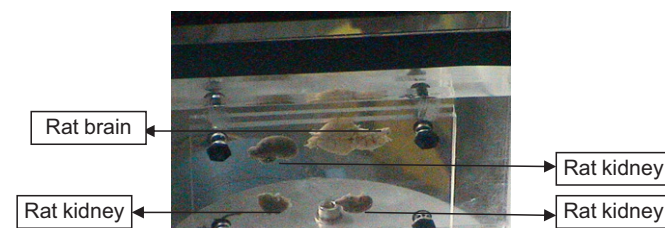

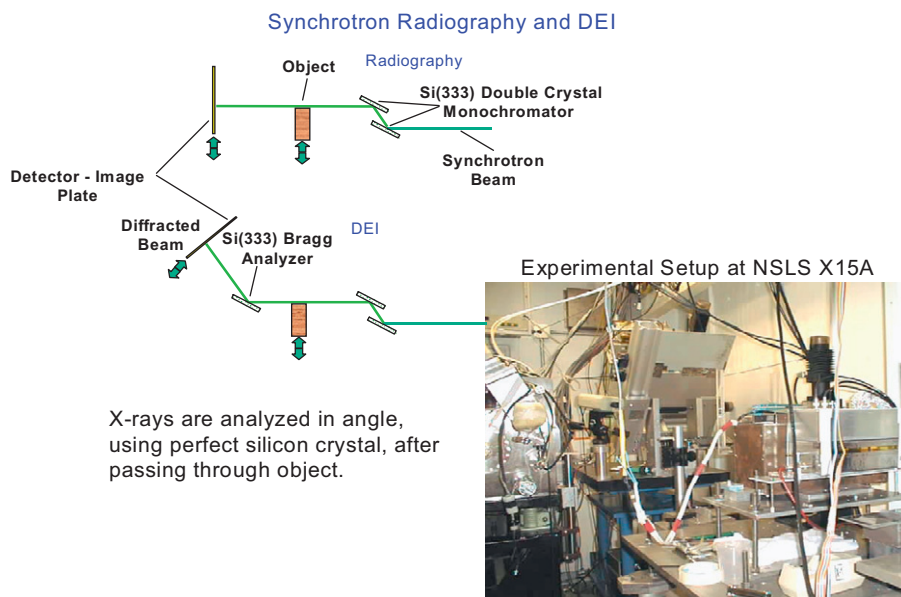**Fig. 4.** Fixation of the rat kidney and rat brain in Perspex containers filled with water.

Fig. 2. Schematic diagram of DEI imaging apparatus at beamline X-15, to acquire the images.
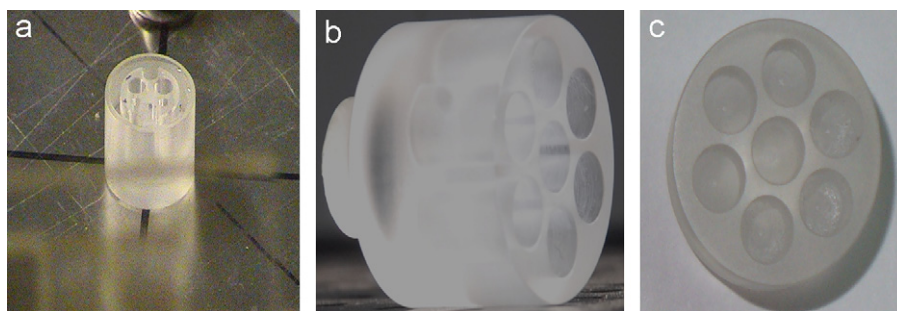

Fig. 3. Photographs of the phantom (a) brain phantom (b) cylindrical phantom, and (c) cylindrical phantom (top view).

angles. As the analyzer crystal is rotated about a horizontal plane, the crystal will go through a Bragg condition for diffraction and the diffracted intensity will trace out a profile or a rocking curve. The rocking curve of the analyzer in the protocol described here is roughly triangular and has peak intensity close to that of the beam striking in it. The width of this profile is typically a few micro-radians (the full width at half maximum is 3, 2 and 1.5 micro-radians at 20, 30 and 40 keV, using the Si [3,3,3] reflection). This narrow angular width provides the tools necessary to prepare and analyze, on the microradian scale, the angle of X-ray beams modified by the object while traversing it. Since the range of the angles that can be accepted by the analyzer crystal is only a few microradians, the analyzer crystal detects the subject's X-ray scattering (ultra-small-angle-scattering) and refraction of X-rays at the microradian level, an angular sensitivity which is not possible in conventional radiography. The X-ray intensity in the object is therefore modulated by the scattering and refraction properties of the object. To extract refraction information, the analyzer is typically set to the half intensity points on the low $(-)$ and high $(+)$ angle sides of the rocking curve refereed to as -1 and $+1$, respectively, in the following discussion, or at the base of the rocking curve (refereed as -2 and $+2$, respectively, for the low- and high angle sides), while imaging takes place. For acquired images on the positive and negative sides of the curve, the rocking differed by a few percent. This is because the rocking curve has different gradients at low-angle and higher-angle sides. Therefore, the same amount of refraction at each side causes opposite DEI signals.

For optimal extinction (scatter rejection) sensitivity, the ana-lyzer is typically set to the peak of the rocking curve during imaging. In addition, if two images are taken on the steepest slope of the reflectivity, so called absorption image and refraction image can be calculated. Sy-DEI relies on images recorded at well-known positions on the reflectivity curve of the analyzer crystal. The reproducibility of the diffraction-enhanced images is main-tained by monitoring the intensity of the diffracted X-rays by the analyzer just prior to imaging to ensure that the analyzer is at the prescribed angular position. The refraction contrast of the image is evaluated as, $(I-I_0)/I_0$, where 'I' is the intensity of the diffracted beam by the analyzer and 'I_0' be the intensity of the directly transmitted beam (without refraction) through the sample and then diffracted by the analyzer.

2.2. Phantoms dimensions and sample

The brain phantom has 20 mm diameter and 15 mm height, with a wall thickness of 1 mm, and was grooved, with an internal channel having vertical height of 10 mm. In the middle, we designed and fabricated a phantom, with two curved shapes, and a pair of vertical holes with 3 mm and 1 mm diameter, to fill with contrast agents. The cylindrical acrylic phantom has 20 mm diameter and 20 mm height. It has seven vertical holes of 10 mm depth and 4 mm diameter to fill with contrast agents. The bottom has a base of 5 mm height and 10 mm diameter, to fix the phantom in a rigid manner. We prepared the rat kidney and rat brain with standard procedure and guidelines. Rat kidney and rat brain samples were prepared from adult Sprague-Dawley rats. All the experimental protocols involving the use of animals were approved in compliance with the Institutional Animal Care and Use Committee guidelines.

2.3. Contrast agents

Phantoms filled with contrast agents were used to see pure diffraction enhancement signal with water, physiological saline and iodine for comparison purposes. The iodine contrast agent

increases the absorption of X-rays and this leads to better resolution of internal structures. However, an iodine contrast agent with various demerits, such as high viscosity, high osmo-larity and allergenicity, causes adverse reactions, sometimes resulting in death (Katayama et al., 1990). Since, in phase-contrast X-ray imaging, light elements cause a sufficient phase shift, contrast agents without iodine is a good choice. Physiological saline had the highest contrast enhancement, and enabled clear imaging of the vessels in the excised liver of rats, so it was selected for use as the contrast agent of the vessels (Takeda et al., 2002). Physiological saline composed of sodium chloride without iodine has excellent merits for vessel imaging because the osmolarity and viscosity are reduced by one-half to one-third and one-thirteenth to one quarter, respectively, compared with iodine contrast agent. Based on above, physiological saline has been used for phase-contrast X-ray imaging of the vessel, and this was compared with absorption-contrast x-ray images (Takeda et al., 2012). In between, water is a standard choice in all the experimental studies. Water and the saline enhanced the diffrac-tion signal.

2.4. Tomography

For tomographic reconstruction, a filtered back projection algorithm was used (Herman, 2009). Custom programs written in Interactive Data Language (IDL) were used to perform all of the image analysis, tomographic reconstructions and graphic visuali-zation. The resolution of the detector is 9 μm but the reconstruc-tion was performed with 2×2 rebinning to achieve a voxel size of 18 μm. The raw tomography projections were transformed to sinogram for image reconstruction.

2.5. Data analysis

Depending on the current of the storage ring, the radiation exposure to the subject was measured with an ion chamber and maintained by adjusting the speed of each scan. All scans are controlled by PC running the SPEC experimental control program. Macros were specially written to control the diffraction-enhanced imaging experiment. The program obtains from the user the type of the scan, scan range and other analyzer's position through the stepper motors. The program also monitors the ion-chamber response throughout the scan to obtain dose information and controls the shutter. The radiation exposure to the specimen was 1.6 milli-grays per planar image, over an exposure time of approximately 30 s to cover an image area of 24 mm by 36 mm. For SY-DEI-CT, the exposure was between 0.1 Gy (40 keV) and 1 Gy (20 keV) using 1 s exposure time per rotation and 1000 rotations. The flux measured by the ion chamber ranges from 10^7 to 10^8 photons/s/mm^2, depending on the ring current and X-ray energy. The scan speed is of the order of 1 mm/s. The exposure on the detector ranged from 10^3 to 10^4 photons/pixel depending on the analyzer's position. Dark current images are taken with the shutter closed.

3. Results and discussion

For the planar Sy-DEI imaging, the sample stage scanned the object vertically through the X-ray beam. Planar Sy-DEI images were processed using the background subtraction tool in Image Pro Express 5.1 (Media Cybernetics, Bethesda, MD). For planar imaging, we acquired 21 images at different analyzer positions for each sample. Sy-DEI planar images are shown in Figs. (5–10). Figs. 5(a) to 7(b) show the images of the rat kidney acquired on both sides of the rocking curve, at 20, 30 and 40 keV. The brighter
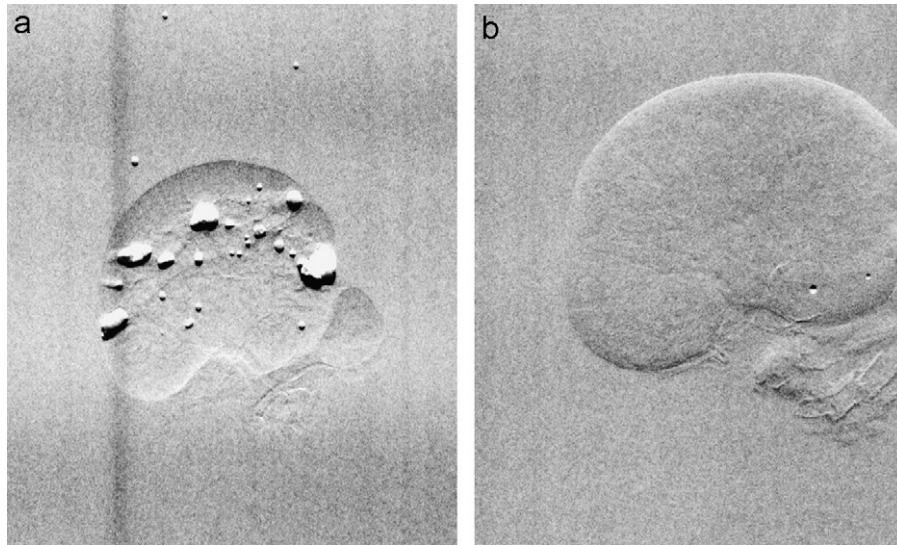
Fig. 5. (a) and (b) Diffraction-enhanced images of the rat kidney with 20 keV [3,3,3] [(a) −ve side of the rocking curve (b) +ve side of the rocking curve].
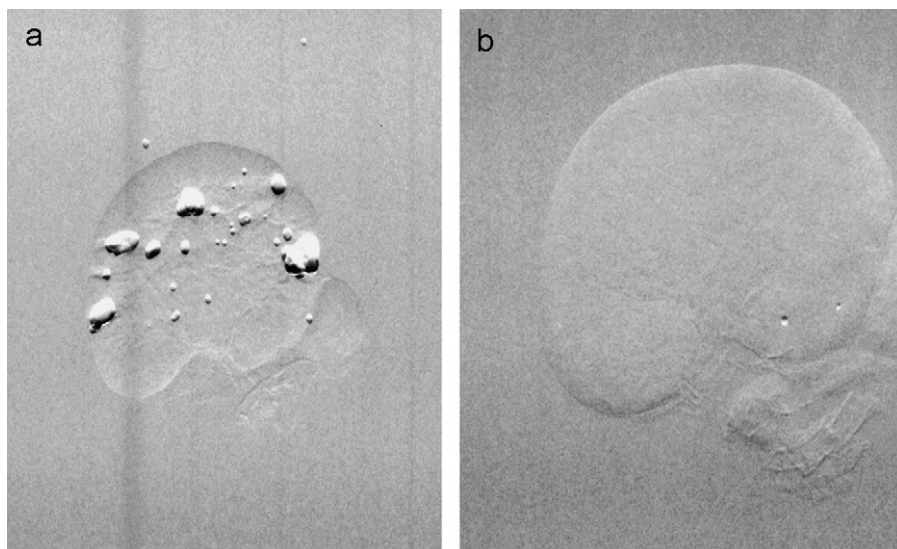

Fig. 6. (a) and (b) Diffraction-enhanced images of the rat kidney with 30 keV [3,3,3] [(a) −ve side of the rocking curve (b) +ve side of the rocking curve].
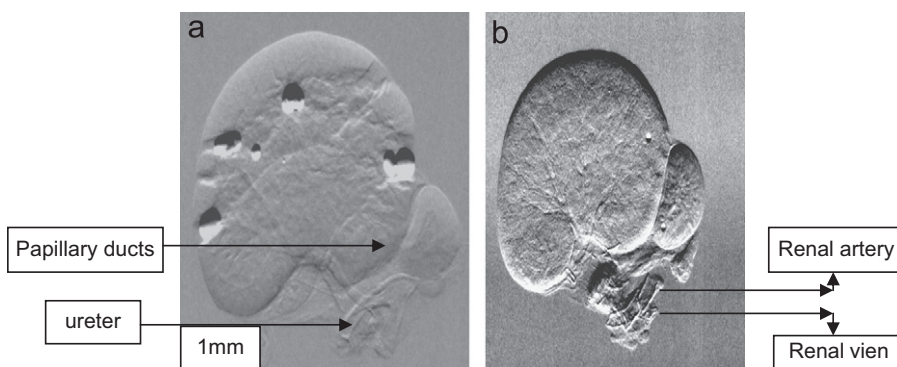

Fig. 7. (a) and (b) Diffraction-enhanced images of the rat kidney with 40 keV [3,3,3] [(a) −ve side of the rocking curve (b) +ve side of the rocking curve].

area in the images represents the low X-ray intensity or more apparent absorption. In order to check the analyzer crystal settings, acquired the images at different scans. As such no significant variation in the stability of the system during the acquisition of the diffraction-enhanced images. At this stage, diffraction-enhanced images are acquired on (−ve) and (+ve) side of the rocking curve. Many anatomical structures of rat kidney are clearly visible at 20, 30 and 40 keV with water as contrast agent. However, the contrast is much better at 40 keV with anatomical features, in view of this we consider this energy
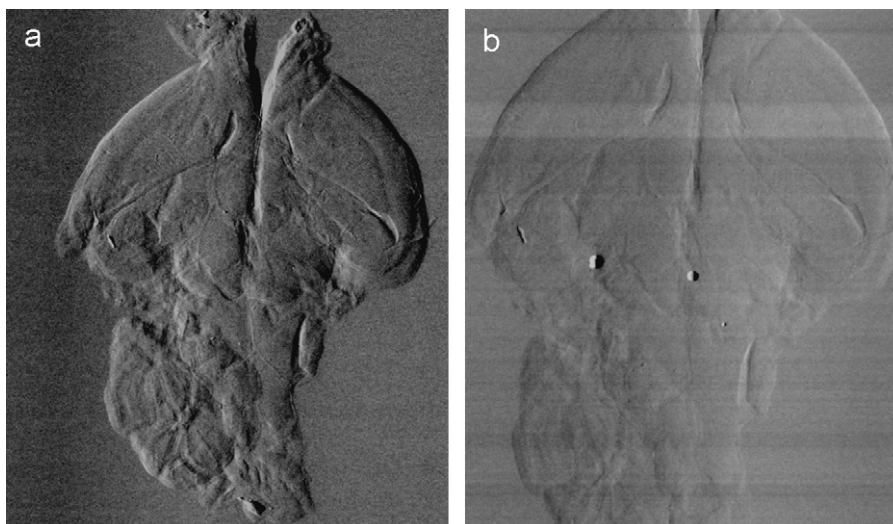
Fig. 8. Diffraction-enhanced images of rat brain with 20 keV [3,3,3] [(a) −ve side of the rocking curve (b) +ve side of the rocking curve].
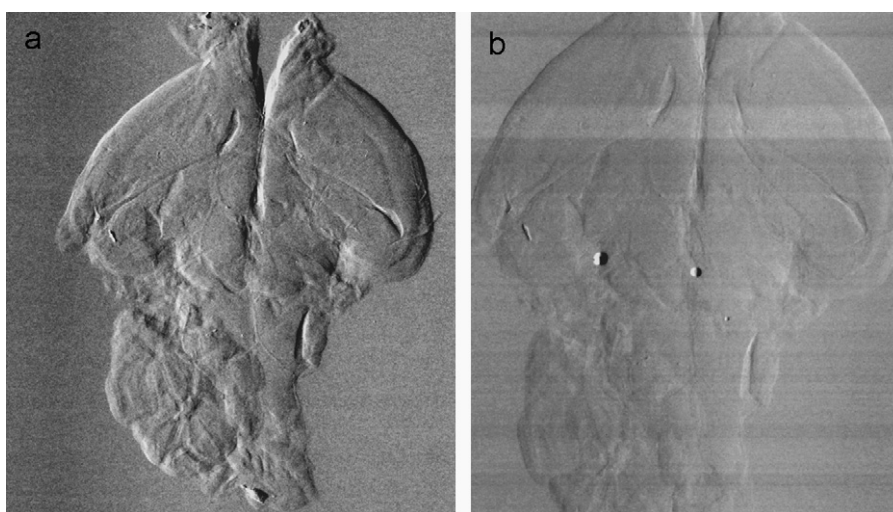

Fig. 9. Diffraction-enhanced images of rat brain with 30 keV [3,3,3] [(a) −ve side of the rocking curve (b) +ve side of the rocking curve].
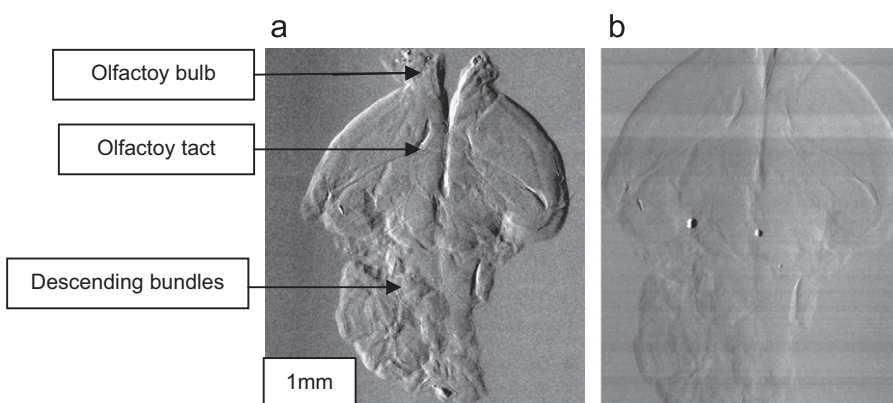

Fig. 10. Diffraction-enhanced images of rat brain with 40 keV [3,3,3]. [(a) −ve side of the rocking curve (b) +ve side of the rocking curve].

is a good choice compared to 20 and 30 keV. At 40 keV, the region of ureter and fine structural features of papillary ducts are intact with reasonable visibility, on the (−ve) side of the rocking curve (Fig. 6(a)) and renal artery and rein vein on the (+ve) side of the rocking curve (Fig. 7(b)). Figs. 8(a) to 10(b) show the images of the rat brain on both sides of the rocking curve, as obtained in the above manner at 20, 30 and 40 keV. Olfactory bulb and cortex are clearly distinguishable in rat brain images with much contrast and the mid-brain and cerebellum are mixed. Olfactory bulb, olfactory tact, descending bundles and few other details are visible with improved contrast at 40 keV, on the (−ve) side of the rocking curve (Fig. 10(a)) as distinguished from the images of

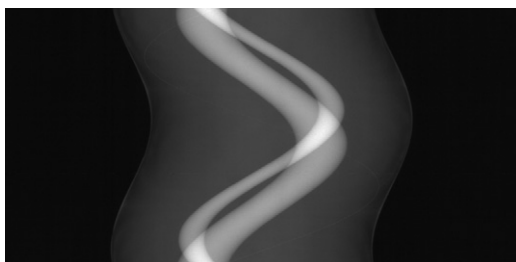**Fig. 11.** A slice of the raw data from a projection at 40 keV.

Fig. 12. Sinogram above iodine K-edge.

Fig. 13. Sinogram below iodine K-edge of a cylindrical phantom of a cylindrical phantom.

20 and 30 keV. These refraction images give a clear identification and visibility of the structures with considerable degree of level of detail present. This way, Sy-DEI system reliably detects, resolve the fine structural features and patterns of the ray kidney and rat brain.

Two sets of Sy-DEI-CT scans were performed for each phantom by fixing the analyzer crystal at a specific angle and rotating the sample stepwise through 360° at 0.5° or 18° increment. The specific angle for the analyzer crystal is fixed at 17.26°, 11.62° and 8.56° for 20, 30 and 40 keV. The phantoms are filled with contrast agents, such as water, physiological saline and iodine. Due to the nearly equal values of mass attenuation coefficients of water and Lucite, the reconstructed images will not show apparent absorption differences. For each scan, three types of data were collected; these were background, air and actual image. The background image was for obtaining information about detector artifacts. The air image was for obtaining information about attenuation by air. Therefore, X-rays are projected to the detector without the phantom in the beam. Twenty sets of the background and air images were taken, for each image set. Averaged values for these were used to analyze data in the following way. The actual image is for obtaining information about the phantoms. For each Sy-DEI-CT image, 720 or 2000 projections were acquired with a sample rotation step size of 0.5° or 0.18°, and with an acquisition time of 1 s per image.

A slice of the raw data from a projection is shown in Fig. 11. Figs. 12 and 13 show the sinogram's of the cylindrical test phantom above and below the iodine K-absorption edge. The outer channel in the brain phantom and the holes in the cylindrical phantom are filled with varying percentage of 1–15 mg/ml of iodine. Figs. 14 and 15 show the images of a small brain phantom with contrast agents above and below the K-absorption edge, filled with iodine and physiological saline. For these phantoms, the analyzer was set at 10.27° and 10.33°, above (33.269 keV) and below (33.069 keV) iodine K-absorption edge. Above the K-absorption edge (Fig. 14), larger hole filled with iodine has less contrast, compared to the smaller hole with filled physiological saline. Below the K-absorption edge (Fig. 15), the larger hole has higher contrast, compared the smaller hole with physiological saline. Figs. 16 and 17 show the images of the brain phantom, filled with iodine in the internal channel, water and physiological saline, within the holes of different diameter, to assess the image contrast, above and below the K-absorption edge. The percentage of refraction contrast varies from 0.1 to 3.5% for 1–15 mg/ml of iodine. Above and below the K-absorption edge, the outer region filled with iodine has better contrast, dominating the holes with filled with water and physiological saline. An increase in image contrast is observed between the
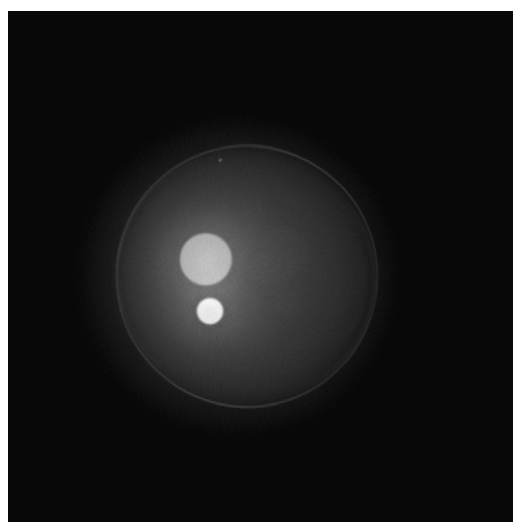

Fig. 14. Phantom image above iodine K-edge of a brain phantom [Small hole: Filled with physiological saline: Larger hole: Filled with iodine].
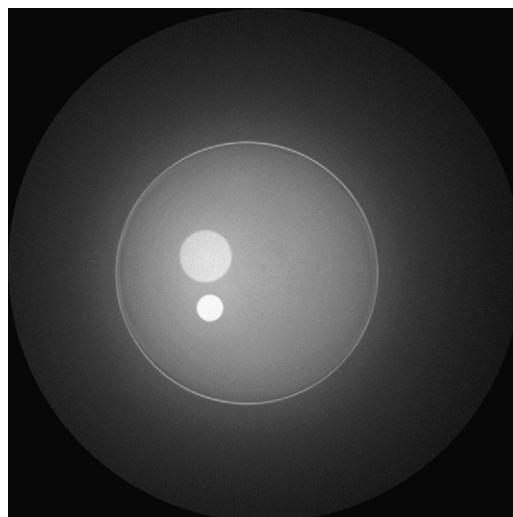

Fig. 15. Phantom image below iodine K-edge of a brain phantom [Small hole: Filled with physiological saline: Larger hole: Filled with iodine].

images acquired above and below the iodine K-edge. Extinction contrast was examined at 20, 30 and 40 keV by tuning the analyzer towards the peak of the rocking curve. At 40 keV
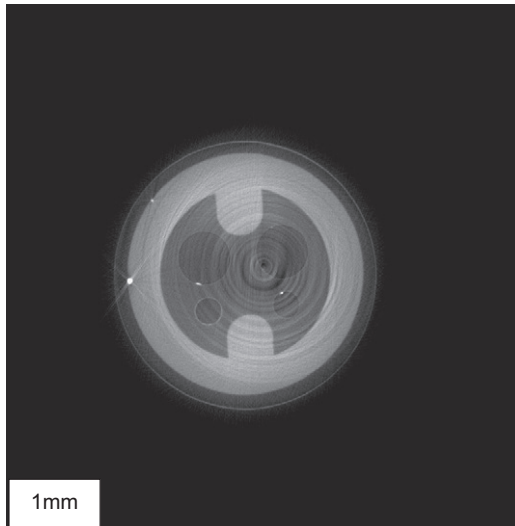
Fig. 16. Brain phantom image above iodine K-edge [Inner channel filled with iodine and internal holes filled with physiological saline].
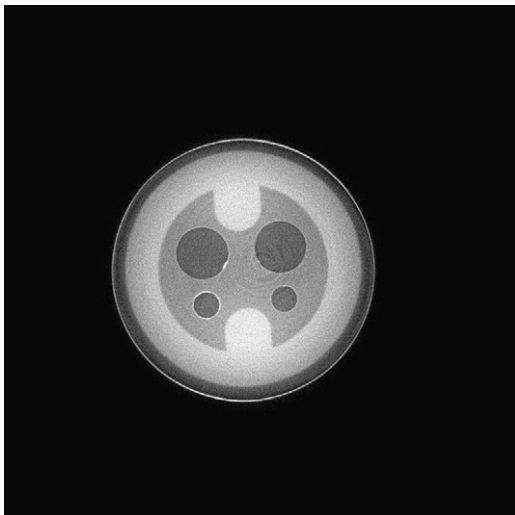

Fig. 17. Brain phantom image below iodine K-edge [Inner channel filled with iodine and internal holes filled with physiological saline].

considerable extinction contrast has been achieved, compared to 20 and 30 keV. This suggests that 40 keV, is a good choice supporting the earlier investigations, related to soft-tissue imaging (Rao et al., 2010a).

The contrast is much better with iodine, above and below the K-absorption edge, as distinguished from physiological saline and water, for the brain phantom and cylindrical phantom. The inner holes of the brain phantom, having diameters of 1 mm and 3 mm, are filled with iodine and physiological saline. The brain phantom with iodine inside the channel provided improved contrast, compared to water and physiological saline, below the K-absorption edge. The trend is similar in the case of cylindrical phantom below the K-absorption edge. The diffraction-enhanced image with iodine show considerable contrast, when compared to the physiological saline. But the overall diffraction-enhanced image features are similar, both below and above the K-absorption edge. The images have much visibility of differentiation with contrast agents and acceptability of Sy-DEI-CT for soft material imaging with improved image quality. Images acquired in Sy-DEI-CT mode, reflect the current knowledge of improvements related to soft materials and relatively to similar measurements. The

Sy-DEI-CT technique provides excellent contrast and fine detail visibility, while field of view is not a substantial problem with planar DEI, limited field of view is much more important for Sy-DEI-CT to avoid problems for imaging major regions of interest. Images acquired in Sy-DEI-CT mode with contrast agents may provide new information for comparison purposes for contrast evaluation. The contrast agents causes increased X-ray absorption and this reflects on contrast enhancement.

4. Conclusions

Investigated the possibilities of Sy-DEI to image complex biological specimens, such as rat kidney and rat brain and Sy-DEI-CT system to image small test phantoms with contrast agents, to enhance the contrast.

Sy-DEI provided high resolution images acquired on both sides of the rocking curve with improved contrast and clear visibility of the anatomical structures. Sy-DEI-CT images yielded high-contrast and high-resolution images with iodine, water, and physiological saline.

References

Antunes, A., Safatle, A., Barros, P., Morelhao, S., 2006. X-ray imaging in advanced studies of ophthalmic diseases. Med. Phys. 33, 2338–2343.

Brankov, J., Wernick, M., Yang, Y., Li, J., Muehleman, C., Zhong, Z., Anastasio, M., 2006. A computed tomography implementation of multiple-image radiography. Med. Phys. 33, 278–289.

Chapman, D., Pisano, E., Thomlinson, W., Zhong, Z., Johnston, R.E., Washburn, D., Sayers, D., 1998. Medical and biological applications of diffraction enhanced imaging. Breast Dis. 10, 197–207.

Chapman, D., Thomlinson, W., Johnston, R.E., Washburn, D., Pisano, E., Gmür, N., Zhong, Z., Menk, R., Arfelli, F., Sayers, D., 1997. Diffraction enhanced x-ray imaging. Phys. Med. Biol. 42, 2015–2025.

Chou, C., Anastasio, M., Brankov, J., Wernick, M., Brey, E., Connor Jr, D., Zhong, Z., 2007. An extended diffraction-enhanced imaging method for implementing multiple-image radiography. Phys. Med. Biol. 52, 1923–1945.

Connor, D., Sayers, D., Sumner, D., Zhong, Z., 2006. Diffraction enhanced imaging of controlled defects within bone, including bone–metal gaps. Phys. Med. Biol. 51, 3283–3300.

Dilmanian, F.A., Zhong, Z., Ren, B., Wu, X.Y., Chapman, L.D., Orion, I., Thomlinson, W.C., 2000. Computed tomography of X-ray index of refraction using the diffraction-enhanced imaging method. Phys. Med. Biol. 45, 933–946.

Fitzgerald, R., 2000. Phase-sensitive X-ray imaging. Phys. Today 53, 23–26.

Hasnah, M., Zhong, Z., Parham, C., Zhang, H., Chapman, D., 2007. Crystal tilt error and its correction in diffraction enhanced imaging system. Nucl. Instrum. Methods A 572, 953–957.

Herman, G.T., 2009. Fundamentals of Computerized Tomography: Image Reconstruction from Projection, 2009, 2nd edition Springer.

Hubbell, J.H., andSeltzer, S.M., 1996. Tables of X-ray Mass Attenuation Coefficients and Mass Energy-Absorption Coefficients. ⟨http://physics.nist.gov./PhysRef Data/XrayMassCoef/cover⟩.

Katayama, H., Yamaguchi, K., Kozuka, T., Takashima, T., Seez, P., Matsuura, K., 1990. Adverse reactions to ionic and nonionic contrast media. A report from the Japanese committee on the safety of contrast media. Radiology 175, 621–628.

Kelly, M., Beavis, R., Fourney, D., Schultke, E., Parham, C., Juurlink, B., Zhong, Z., Chapman, L., 2006. Diffraction-enhanced imaging of the rat spine. Can. Assoc. Radiol. J. 57, 204–210.

Khelashvili, G., Brankov, J., Chapman, D., Anastasio, M., Yang, Y., Zhong, Z., Wernick, M., 2006. A physical model of multiple-image radiography. Phys. Med. Biol. 51, 221–236.

Kim, C., Bourham, M., Doster, J., 2006. A wide-beam X-ray source suitable for diffraction enhanced imaging applications. Nucl. Instrum. Methods A 566, 713–721.

Kiss, M.Z., Sayers, D.E., Zhong, Z., Parham, C., Pisani, E., 2004. Improved image contrast of calcifications in breast tissue specimens using diffraction enhanced imaging. Phys. Med. Biol. 49, 3427–3439.

Lewis, R.A., Hall, C.J., Hufton, A.P., Evans, S., Menk, R.H., Arfelli, F., Rigon, L., Tromba, G., Dance, D.R., Ellis, I.O., Evans, A., Jacobs, E., Pinder, S.E., Rogers, K.D., 2003. X-ray refraction effects: application to the imaging of the biological tissues. Br. J. Radiol. 76, 301–308.

Li, J., Zhong, Z., Litdke, R., Kuettner, K., Peterfy, C., Aleyeva, E., Muehleman, C., 2003. Radiography of soft tissue of the foot and ankle with diffraction enhanced imaging. J. Anatom. 202, 463–470.

Muehleman, C., Chapman, L.D., Kuettner, K.E., Rieff, J., Mollenhauer, J.A., Massuda, K., Zhong, Z., 2003. Radiography of rabbit articular cartilage with diffraction enhanced imaging. Anat. Rec. Part A 272A, 392–397.

Muehleman, C., Li, J., Zhong, Z., 2006. Preliminary study on diffraction enhanced radiographic imaging for a canine model of cartilage damage Osteoarthr. Cartilage 14, 882–888.

Muehleman, C., Li, J., Zhong, Z., Brankov Jand Wernick, M., 2006. Multiple-image radiography for human soft tissue. J. Anat. 208, 115–124.

Oltulu, O., Zhong, Z., Hasnah, M., Wernick, M.N., Chapman, D., 2003. Multiple image radiography in diffraction enhanced imaging. J. Phys. D: Appl. Phys. 36, 2152–2156.

Rao, D.V., Akatsuka, T., Tromba, G., 2003. Images of Soft Bodied Animals with External Hard Shell. A 3D Visualization of the Embedded Soft Tissue. Presented at Eighth International Conference on Synchrotron Radiation Instrumentation, August 25–29, 2003, San Francisco, USA. AIP Proceedings, Vol. 705, pp. 1308–1311.

Rao, D.V., Yuasa, T., Akatsuka, T., Zhong, Z., Tromba, G., Takeda, T., 2005. X-ray CT and DEI Images of the Biological Soft-Tissue using Synchrotron X-rays. Presented at XRM 2005, 26–30th July, Egret, Himeji, Japan.

Rao, D.V., Yuasa, T., Akatsuka, T., Zhong, Z., Tromba, G., Takeda, T., 2005a. Images of the Rat Bone and Lumber Vertebra using Diffraction-Enhanced Imaging Technique. Presented at XRM 2005a, 26–30th July, Egret, Himeji, Japan.

Rao, D.V., Zhong, Z. Tromba, G., 2007. Utilization of Diffraction-Enhanced Imaging Technique for Soft-Tissue Imaging 15th VUVXV, July 29th–August 3rd, 2007, Berlin, Germany.

Rao, D.V., Cesareo, R., Brunetti, A., Zhong, Z., Akatsuka, T., Yuasa, Y., Takeda, T., Gigante, G.E., 2010. Cork embedded internal features and contrast mechanisms with DEI using 18, 20, 30, 36 and 40 keV synchrotron X-rays. Res. Nondestr. Eval. 21 (3), 171–183.

Rao, D.V., Swapna, M., Cesareo, R., Brunetti, A., Zhong, Z., Akatsuka, A., Yuasa, Y., Takeda, T., Gigante, G.E., 2010a. Use of synchrotron-based diffraction-enhanced imaging for visualization of soft tissues in invertebrates. Appl. Radiat. Isot. 68, 1687–1693.

Thomlinson, W., Chapman, D., Zhong, Z., Johnston, R., Sayers, D., 1998. Diffraction Enhanced X-ray imaging Medical Applications of Synchrotron Radiation. In: Ando, M., Uyama, C. (Eds.), Springer, Tokyo, pp. 72–77.

Takeda, T., Yoneyama, A., Wu, J., Thet-Thet, Lwin, Momose, A., Hyodo, K., 2012. In vivo physiological saline-infused hepatic vessel imaging using a two-crystal-interferometer-based phase-contrast X-ray technique. J. Synchrotron Radiat. 19, 252–256.

Takeda, T., Momose, A., Wu, J., YQ., Zeniya, T., Thet-Thet, Lwin, Yoneyama, A., Itai, Y., 2002. Vessel imaging by interferometric phase-contrast X-ray technique. Circulation 105, 1708–1712.

Wernick, M., Yang, Y., Mondal, I., Chapman, D., Hasnah, M., Parham, C., Pisano, E., Zhong, Z., 2006. Computation of mass-density images from x-ray refraction-angle images. Phys. Med. Biol. 51, 1769–1778.

Wilkins, S.W., Gureyev, T.E., Gao, D., Pogany, A., Stevenson, A.W., 1996. Phase-contrast imaging using polychromatic hard X-rays. Nature 384, 335–338.

Young, L.W., Parham, C., Zhong, Z., Chapman, D., Reaney Martin, J.T., 2007. Non-destructive diffraction enhanced imaging of seeds. J. Exp. Bot. 58 (10), 2513–2523.

Zhong, Z., Chapman, D., Menk, R., Richardson, J., Theophanis, S., Thomlinson, W., 1997. Monochromatic energy-subtraction radiography using a rotating anode source and a bent Laue monochromator. Phys. Med. Biol. 42, 1751–1762.

Zhong, Z., Thomlinson, W., Chapman, D., Sayers, D., 2000. Implementation of diffraction-enhanced imaging experiments at the NSLS and APS. Nucl. Instrum. Methods A 450, 556–567.